JOURNAL OF AEROSPACE COMPUTING, INFORMATION, AND COMMUNICATION
Vol. 6, March 2009

Vision-Based Landing of Fixed-Wing Miniature Air Vehicles

Blake Barber*
Procerus Technologies, Vineyard, UT 84058

and

Timothy McLain† and Barrett Edwards‡
Brigham Young University, Provo, UT 84602

DOI: 10.2514/1.36201

This paper outlines a method for using vision-based feedback to land a miniature air vehicle accurately on a visually identifiable target of approximately known location. The method presented is robust to wind, capable of handling both stationary and moving targets, and capable of correcting for camera misalignment, state estimation biases, and parameter estimation biases. Landing results from actual flight tests are presented that demonstrate the effectiveness of the proposed method.

I. Introduction

FIXED-WING miniature air vehicles (MAVs) have garnered much attention recently for their usefulness in both civil and military applications. MAVs have primarily been deployed as short-range aerial reconnaissance vehicles. In this role, MAVs are used to collect information that is passed on to other agents, which subsequently must spend time navigating to the target site before any action can be taken. However, in many circumstances it would be desirable to have the MAV take action immediately rather than waiting for other agents.

An example of such a scenario is a search and rescue mission. Typically, MAVs would be used quickly to comb a search area, locating the lost individual and directing search teams into the target region. In many instances, however, it may be beneficial to take immediate action rather than waiting for ground-based agents. For instance, some of the searching MAVs may carry food, medicine, or a communication device such as a two-way radio. It would be desirable to deliver this payload accurately to a target region in plain sight of the lost individual. Another such mission is convoy protection, in which a team of MAVs is used to identify and monitor threats to a convoy moving through hostile terrain. Clearly in this situation once a threat is identified it would be desirable to take action as quickly as possible.

We will refer to missions such as these, in which the MAV is used to search for and deliver a payload to a target site, as search and engage missions. This paper will focus on the engagement part of this mission. In previous work, we have demonstrated the ability to use hand-launched MAVs to geolocate objects of interest to within 2 to 5 m in high wind conditions [1]. The same methods have been used in more recent testing to estimate both target position and velocity with high accuracy. In this work, it is assumed that the engaging MAV has access to measurements of target position and velocity from a searching MAV. These measurements will be used to assist the engaging MAV to accurately deliver an attached payload to the target site. Accurate landing at the target site makes use of the noisy

Received 13 December 2007; revision received 01 October 2009; accepted for publication 24 November 2008.

* Procerus Technologies, blakeb@procerusuav.com
† Brigham Young University, mclain@byu.edu
‡ Brigham Young University, barrettedwards@byu.edu

position and velocity estimates initially, but then uses vision-based control once the target has been acquired in the engaging MAV's field of view.

The problem of accurately landing an unmanned air vehicle (UAV) using vision-based control has been well studied for autonomous rotorcraft [2–5]. Most of these approaches use structure from motion algorithms and require a structured landing environment. A method that does not require a structured landing environment has been developed by researchers at the Army/NASA Rotorcraft Division [6,7].

Techniques for the landing of rotorcraft, however, rely on the ability to hover and thus do not transition well to fixed-wing platforms. Significantly less work exists for using visual sensors to land fixed-wing aircraft accurately. Those techniques that have been developed generally require a set of known landmarks or some visually identifiable pattern [8,9]. The vision-based landing method developed in this work does not require the presence of any such landmarks or markings.

An alternative vision-based approach for accurately landing fixed-wing aircraft without the need for landmarks involves the use of a dedicated visual sensor for measuring optic flow. In [10], Chahl et al. demonstrate that by maintaining constant optic flow during a landing maneuver, a MAV's descent can be successfully controlled. Development of lightweight sensors for measurement of optic flow [11–13] has further validated this approach. Barrows et al. have demonstrated that these sensors can be successfully used to follow terrain in low flying MAVs [14].

This work builds on previous work done at Brigham Young University (BYU) in which vector-field based control is combined with optic flow measurements to accurately land a MAV [15]. This work will use the landing algorithm outlined in [15] to guide the approach of the MAV until the target is visually acquired. At this point, the control is turned over to the vision-based controller outlined in the remainder of this paper.

The vision-based control approach is preferred over the use of dedicated optic flow sensors because it transitions better to search and engage missions: it allows for moving targets, and it is robust to errors in the initial estimate of target location. The approach to vision-based control taken in this paper combines a feedback loop based on the observed pixel coordinates of the target with an adaptive bias correction. This control scheme is shown schematically in Fig. 1.

The remainder of this paper is organized as follows: Sec. II contains a description of the longitudinal control, focusing on the effects of bias errors on the performance of the control law. Section III discusses the effect of wind and introduces a method for accounting for wind in the longitudinal control. Section IV explains how to account for moving targets using a "pseudo-wind" and the methods outlined in Sec. III. Section V extends the ideas developed for longitudinal control to lateral control. Section VI combines the lateral and longitudinal control laws. Section VII outlines the addition of adaptive counter-bias terms to the feedback control law developed in Sec. VI. Section VIII gives hardware results demonstrating successful landing on both stationary and moving targets. Finally, the paper ends with conclusions in Sec. IX.

II. Two-Dimensional Model for Longitudinal Control

In this paper, it is assumed that the user selects the nominal linear glideslope that is best-suited to their mission needs. Where the survival of the MAV is a concern the user should specify a shallower glideslope that keeps airspeeds low. If the survival of the MAV is not a concern it may be beneficial to select a steeper glideslope to clear any vertical obstructions. In either case selection of the nominal glideslope is both platform and mission dependent and is not addressed.

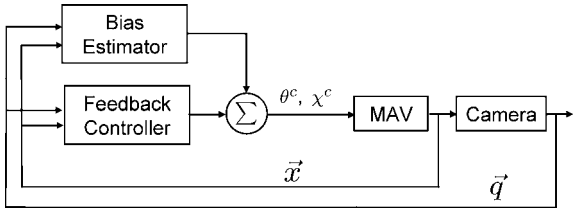

Fig. 1 Diagram of the control scheme outlined in this paper.

Accurately tracking a linear glideslope to a target point requires aligning the motion vector of the MAV with the position vector $\boldsymbol{p}$ extending from the MAV to the target. A unit vector in the direction of $\boldsymbol{p}$, denoted by $\boldsymbol{u}_{\mathbf{p}}$, can be found using the pixel coordinates of the target in the image and the coordinate transformations outlined in [1]. Once $\boldsymbol{u}_{\mathbf{p}}$ has been determined, the next step is to align the MAV's motion vector. However, both the process of calculating $\boldsymbol{u}_{\mathbf{p}}$ and aligning the MAVs motion vector with $\boldsymbol{u}_{\mathbf{p}}$ are subject to bias errors owing to camera misalignment as well as parameter and state estimation errors. These bias errors tend to be relatively large for MAVs owing to the relatively low sensor quality and the impracticality of precision mounting on these small, low-cost platforms. Because these bias errors are relatively large they tend to have a much greater effect on system performance than the zero-mean random disturbances. Because of this it is important to understand the overall effects of these biases on landing accuracy.

To examine these effects, consider the following simplified two-dimensional (2D) model for the longitudinal dynamics of the MAV in the absence of wind

$$\dot{x} = V_{\mathrm{a}} \cos(\theta - \alpha) \tag{1}$$

$$\dot{h} = V_{\mathrm{a}} \sin(\theta - \alpha). \tag{2}$$

In Eqs (1) and (2) h and x are defined by the earth-fixed coordinate frame shown in Fig. 2, V_{a} is the airspeed of the MAV, θ is the pitch, and α is the angle of attack. V_{a} is treated as an input to the system and is maintained constant. θ is also treated as an input to the system and is set according to the control law

$$\theta^c = \hat{\gamma}_{\mathrm{tgt}} + \hat{\alpha} \tag{3}$$

where $\hat{\gamma}_{\mathrm{tgt}}$ represents the estimate of the angle between the ray from the MAV to the target, and the ground as shown in Fig. 2, and $\hat{\alpha}$ represents the estimate of the MAV's angle of attack.

The value of $\hat{\gamma}_{\mathrm{tgt}}$ is given by the four quadrant inverse tangent of the components of $\boldsymbol{u}_{\mathbf{p}}$ plus the relative orientation estimation error $\tilde{\gamma}_{\mathrm{tgt}}$. That is

$$\hat{\gamma}_{\mathrm{tgt}} = \mathrm{atan2}(u_{\mathrm{p}h}, u_{\mathrm{p}x}) + \tilde{\gamma}_{\mathrm{tgt}}. \tag{4}$$

Similarly, the value of $\hat{\alpha}$ is given by

$$\hat{\alpha} = \alpha + \tilde{\alpha} \tag{5}$$

where $\tilde{\alpha}$ represents the error in the estimation of the angle of attack.

Substituting Eqs (4) and (5) into Eq. (3) gives

$$\theta^c = \mathrm{atan2}(u_{\mathrm{p}h}, u_{\mathrm{p}x}) + \alpha + \tilde{\gamma}_{\mathrm{tgt}} + \tilde{\alpha} \tag{6}$$

Combining the error terms and replacing them with the new variable $\tilde{\theta}$ gives

$$\theta^c = \mathrm{atan2}(u_{\mathrm{p}h}, u_{\mathrm{p}x}) + \alpha + \tilde{\theta} \tag{7}$$

Replacing θ in the dynamic model given by Eqs (1) and (2) with this expression for θ^c gives

$$\dot{x} = V_{\mathrm{a}} \cos(\mathrm{atan2}(u_{\mathrm{p}h}, u_{\mathrm{p}x}) + \tilde{\theta}) \tag{8}$$

$$\dot{h} = V_{\mathrm{a}} \sin(\mathrm{atan2}(u_{\mathrm{p}h}, u_{\mathrm{p}x}) + \tilde{\theta}), \tag{9}$$

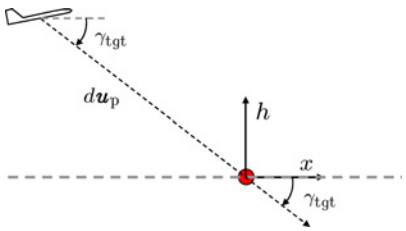

Fig. 2 Two-dimensional longitudinal coordinate system.

.

The combined effect of parameter estimation error, $\tilde{\alpha}$, and relative orientation estimation error, $\tilde{\gamma}_{\text{tgt}}$, can be seen by integrating the equations of motion given in Eqs (8) and (9) for different values of $\tilde{\theta}$. Trajectories corresponding to different values of $\tilde{\theta}$ are shown in Fig. 3 for two different nominal glideslopes.

It can be seen in Fig. 3 that errors in correctly aligning the motion vector of the MAV with the unit vector $\boldsymbol{u}_p$ can cause overshoot or undershoot in the landing location. It is interesting to note, however, that relatively large amounts of error can be tolerated without significant effect on landing position. The sign and magnitude of the error which can be tolerated is a function of the nominal glideslope.

For the case of the steeper nominal glideslope shown in Fig. 3a, the landing trajectory associated with $\tilde{\theta} = -30°$ results in a landing error of approximately 65 m. Undershoot landing error is defined as the distance between the point where the landing trajectory intersects with the ground plane and the desired landing point. For overshoot, the landing error is defined as the distance between the maximum x value of the landing trajectory and the desired landing point. For the case of the more shallow nominal glideslope shown in Fig. 3b, the landing trajectory associated with the same value of $\tilde{\theta}$ results in a landing error of approximately 200 m. However, for $\tilde{\theta} = 30°$ the shallow glideslope gives better results with an overshoot error of approximately 10 m compared to approximately 45 m for the steep glideslope.

The preceding analysis indicates that it may be advantageous to bias the control in either the positive or negative direction depending on the magnitude of the nominal glideslope (shallow glideslopes benefit from positive bias whereas steep glideslopes benefit from negative bias). The magnitude of the desired bias depends on the uncertainty with regards to the magnitude of the true bias $\tilde{\theta}$. Because we may prefer a either a positive or negative bias, we may wish to shift the distribution from which the value of $\tilde{\theta}$ is realized. We can accomplish this by adding an artificial bias term $\bar{\theta}$ to the control law in Eq. (3). This gives

$$\theta^c = \hat{\gamma}_{\text{tgt}} + \hat{\alpha} + \bar{\theta} \tag{10}$$

III. Effects of Wind

The analysis in Sec. II assumes that the wind speed is negligible. In this case, the glideslope angle relative to a coordinate frame fixed to the mass of moving air, γ_{a}, is the same as the glideslope angle relative to a coordinate frame fixed to the ground, γ_{g}. Although this is not generally the case, this simplifying assumption can be made when the wind speed represents a small percentage of the vehicle's airspeed. MAVs, however, typically operate in conditions

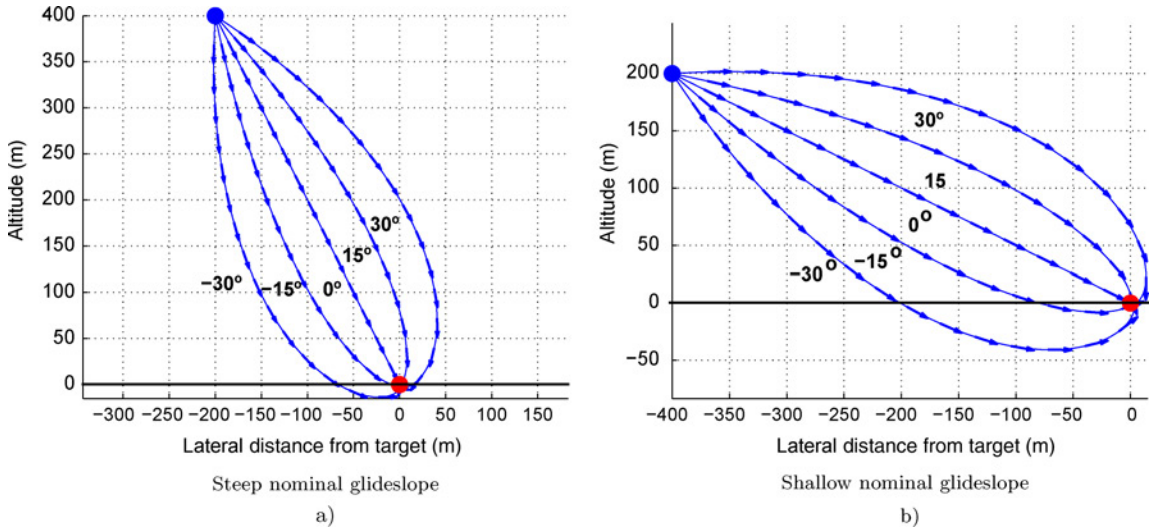

Fig. 3 Effects of nominal glideslope on landing error. In each case the shallowest trajectory corresponds to $\tilde{\theta} = -30°$. The steepest trajectory corresponds to $\tilde{\theta} = 30°$. The intermediate trajectories represent 15 degree increments in $\tilde{\theta}$.

where the wind speed is 10% to 60%, or more, of the commanded airspeed. For this reason, the effects of wind should be accounted for by the control law.

To see the effects of wind, we examine again the simplified 2D longitudinal control law presented in Sec. II. For this analysis we assume a constant wind with a component only in the x direction with magnitude V_{w}. We can then rewrite the dynamic model given by Eqs (1) and (2) as

$$\dot{x} = V_{\mathrm{a}} \cos(\theta - \alpha) + V_{\mathrm{w}} \tag{11}$$

$$\dot{h} = V_{\mathrm{a}} \sin(\theta - \alpha). \tag{12}$$

The goal of the controller is to align the motion vector of the MAV with the estimate of the unit vector in the direction from the MAV to the target, $\hat{\boldsymbol{u}}_{\mathbf{p}}$. In other words, it is desired to set γ_{g} equal to $\hat{\gamma}_{\mathrm{tgt}}$. This can be done by appropriately choosing the value of γ_{a} and setting the input θ^c to achieve this value. Towards this end, the relationships shown in Eqs (11) and (12) can be rewritten as the vector equation

$$\boldsymbol{V}_{\mathbf{g}} = \boldsymbol{V}_{\mathbf{a}} + \boldsymbol{V}_{\mathbf{w}} \tag{13}$$

where

$$\boldsymbol{V}_{\mathbf{g}} = [\dot{x} \quad \dot{h}]^{\mathsf{T}} \tag{14}$$

$$\boldsymbol{V}_{\mathbf{a}} = [V_{\mathrm{a}} \cos(\theta - \alpha) \quad V_{\mathrm{a}} \sin(\theta - \alpha)]^{\mathsf{T}} \tag{15}$$

$$\boldsymbol{V}_{\mathbf{w}} = [V_{\mathrm{w}} \quad 0]^{\mathsf{T}} \tag{16}$$

This vector equation is represented graphically in Fig. 4.

The goal is to align the desired groundspeed vector $\boldsymbol{V}_{\mathbf{g}}^{\mathbf{d}}$ with $\hat{\boldsymbol{u}}_{\mathbf{p}}$. The estimate of the wind vector is given by $\hat{\boldsymbol{V}}_{\mathbf{w}}$ and the magnitude of the airspeed vector V_{a} is an input to the system that is held constant at a known value. The desired groundspeed vector is related to the known quantities by the relationship given in Eq. (13).

Aligning the desired groundspeed vector $\boldsymbol{V}_{\mathbf{g}}^{\mathbf{d}}$ with $\hat{\boldsymbol{u}}_{\mathbf{p}}$ requires finding the value of γ_{a}^d which causes Eq. (13) to be satisfied subject to the constraint

$$\boldsymbol{V}_{\mathbf{g}}^{\mathbf{d}} = V_{\mathrm{g}}^d \hat{\boldsymbol{u}}_{\mathbf{p}} \tag{17}$$

The value of V_{g}^d can be determined by solving for the point of intersection of a line that is collinear with $\hat{\boldsymbol{u}}_{\mathbf{p}}$, and a circle of radius V_{a} centered at the tip of the wind vector. This is represented graphically in Fig. 4.

For convenience, we solve for this point of intersection in terms of a coordinate frame attached to the center of mass of the MAV. In this coordinate frame, the equation for any vector coincident with $\hat{\boldsymbol{u}}_{\mathbf{p}}$ is given by the vector

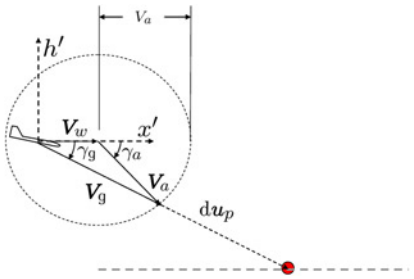

Fig. 4 Graphic representation of the vector relationship described in Eq. (13). The dotted circle has its center at the tip of the wind vector and radius equal to $V_{\mathbf{a}}$.

equation

$$\begin{bmatrix} x' \\ h' \end{bmatrix} = d_1 \hat{\boldsymbol{u}}_{\mathbf{p}} = \begin{bmatrix} d_1 \cdot \hat{u}_{\mathrm{p}x} \\ d_1 \cdot \hat{u}_{\mathrm{p}h} \end{bmatrix} \tag{18}$$

where $\hat{u}_{\mathrm{p}x}$ and $\hat{u}_{\mathrm{p}h}$ represent the x and h components of $\hat{\boldsymbol{u}}_{\mathbf{p}}$, and d_1 is arbitrary. The equation for the circle is given by

$$(x' - \hat{V}_{\mathrm{w}})^2 + h'^2 = V_{\mathrm{a}}^2 \tag{19}$$

The point of intersection can be found by replacing x' and h' in Eq. (19) with the expressions shown in Eq. (18). This gives

$$(d_1 \hat{u}_{\mathrm{p}x} - \hat{V}_{\mathrm{w}})^2 + d_1^2 \hat{u}_{\mathrm{p}h}^2 = V_{\mathrm{a}}^2 \tag{20}$$

Eq. (20) can be solved by finding the positive root of this quadratic equation in the variable d_1. This is given by

$$d_1 = \hat{u}_{\mathrm{p}x} \hat{V}_{\mathrm{w}} + \sqrt{V_{\mathrm{a}}^2 (\hat{u}_{\mathrm{p}x}^2 + \hat{u}_{\mathrm{p}h}^2) - \hat{u}_{\mathrm{p}h}^2 \hat{V}_{\mathrm{w}}^2} \tag{21}$$

The value of d_1 given by Eq. (21) represents the magnitude of the desired groundspeed vector, $\boldsymbol{V}_{\mathrm{g}}^d$. Substituting d_1 into the constraint equation given in Eq. (17) we obtain

$$\boldsymbol{V}_{\mathbf{g}}^{\mathbf{d}} = d_1 \hat{\boldsymbol{u}}_{\mathbf{p}} \tag{22}$$

Once $\boldsymbol{V}_{\mathbf{g}}^{\mathbf{d}}$ has been determined, the desired airspeed vector $\boldsymbol{V}_{\mathbf{a}}^{\mathbf{d}}$ can be found by simple vector arithmetic

$$\boldsymbol{V}_{\mathbf{a}}^{\mathbf{d}} = \boldsymbol{V}_{\mathbf{g}}^{\mathbf{d}} - \hat{\boldsymbol{V}}_{\mathbf{w}} \tag{23}$$

γ_a^d can then be determined from the components of $\boldsymbol{V}_{\mathrm{a}}^{\mathrm{d}}$, $V_{\mathrm{a}x}^d$ and $V_{\mathrm{a}h}^d$, using the relationship

$$\gamma_a^d = \mathrm{atan2}(V_{\mathrm{a}h}^d, V_{\mathrm{a}x}^d) \tag{24}$$

Finally, the control law given in Eq. (10) can be rewritten in terms of γ_{a}^d instead of $\hat{\gamma}_{\mathrm{tgt}}$

$$\theta^c = \gamma_{\mathrm{a}}^d + \hat{\alpha} + \bar{\theta} \tag{25}$$

It is important to note that in addition to the relative orientation errors and parameter estimation errors that affected $\hat{\gamma}_{\mathrm{tgt}}$, γ_{a}^d is also affected by wind estimation errors. This becomes a consideration when selecting the magnitude of the bias term, $\bar{\theta}$.

IV. Effect of Moving Targets

If the reference frame in which x and h are defined is taken to be that of the reference frame attached to the moving target, the effect of target motion is exactly the same as the effect of wind. As such, target motion can be modeled as an additional "pseudo-wind". In this case, target motion in the positive x direction (away from the MAV) can be modeled as a pseudo-wind in the negative x direction (headwind). Similarly, target motion in the negative x direction (toward the MAV) can be modeled as a pseudo-wind in the positive x direction (tailwind). This leads to the following expression for pseudo-wind

$$\bar{\boldsymbol{V}}_{\mathbf{w}} = [(\hat{V}_{\mathrm{w}} - \hat{\dot{x}}_{\mathrm{tgt}}) \quad 0]^{\mathsf{T}} \tag{26}$$

The pseudo-wind, $\bar{\boldsymbol{V}}_{\mathbf{w}}$, can be used in place of $\hat{\boldsymbol{V}}_{\mathbf{w}}$ in the calculations outlined in Sec. III. This results in a controller that is able to track and land on constant-velocity targets as well as stationary targets. It is important to note that in this case the term γ_{a}^d will be affected by target velocity estimation errors as well as the other error sources outlined above. Once again, this becomes a consideration when selecting the magnitude of $\bar{\theta}$.

V. Two-Dimensional Model for Lateral Control

Up to this point, the analysis has dealt strictly with the 2D model for longitudinal control. The extension of these same ideas to 2D lateral control is straightforward. Consider the following model for the lateral dynamics of the MAV in wind

$$\dot{x} = V_g \cos\chi \tag{27}$$

$$\dot{y} = V_g \sin\chi \tag{28}$$

These equations are relative to the coordinate frame shown in Fig. 5. χ is the course of the MAV measured clockwise from the positive x axis and is treated as an input to the system. V_g is not a direct input to the system, but is determined by our choice of V_a and the wind vector $\boldsymbol{V}_w$.

As with the longitudinal control, the goal is to align the motion vector of the MAV with the estimate of the unit vector in the direction from the MAV to the target, $\hat{\boldsymbol{u}}_p$. Because the orientation of the motion vector (χ) is an input to the system, this is trivial. The control law is simply

$$\chi^c = \hat{\chi}_{tgt}, \tag{29}$$

where $\hat{\chi}_{tgt}$ is the estimate of the compass heading from the MAV to the target. The value of $\hat{\chi}_{tgt}$ is given by

$$\hat{\chi}_{tgt} = \text{atan2}(u_{py}, u_{px}) + \tilde{\chi}_{tgt} \tag{30}$$

where $\tilde{\chi}_{tgt}$ represents the relative orientation estimation error in the lateral plane.

An important distinction between the lateral and longitudinal controllers is the effect of parameter estimation errors. Rather than being subject to both relative orientation estimation error and parameter estimation error, the lateral control is only subject to relative orientation estimation error. This error will cause the same type of spiral deviations from the nominal linear trajectory as those shown in Fig. 3. For the longitudinal control, we introduced the bias term $\bar{\theta}$ because there was an advantage to having either an upward or downward spiral depending on the nominal desired glideslope. However, no such advantages or disadvantages exist for having a right-hand versus a left-hand spiral. As such, the lateral control does not benefit from the addition of a similar bias term.

Another important distinction between the lateral control and the longitudinal control is the effect of wind. Unlike the longitudinal control, wind has no effect on the lateral control. This stems from the fact that the lateral equations of motion are written in terms of the system input χ. Because χ is measured relative to a ground-based frame of reference, it is unaffected by wind. However, this is not true for the pseudo-wind introduced in Sec. III to account for moving targets. The pseudo-wind needs to be accounted for in both the lateral and longitudinal control laws. The method for taking the pseudo-wind into account in the lateral control law will be addressed in Sec. VI.

VI. Feedback Control Law

The analysis thus far has dealt strictly with the 2D cases of longitudinal and lateral control. This section extends these same ideas to three dimensions to form the feedback control law represented in the block diagram shown

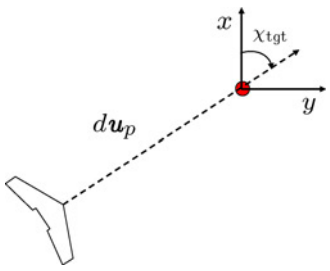

Fig. 5 Two-dimensional lateral coordinate system.

in Fig. 1. The extension of these ideas into three dimensions with simultaneous longitudinal and lateral control is straightforward.

First, we rewrite the equations of motion in three dimensions using the target-centered coordinate frame shown in Fig. 6. For convenience we will continue to write the equations in terms of MAV altitude h using the change of variables $h = -z$. The equations of motion then become

$$\dot{x} = V_{\mathrm{a}} \cos(\theta - \alpha) \cos(\psi) + V_{\mathrm{w}x} \tag{31}$$

$$\dot{y} = V_{\mathrm{a}} \cos(\theta - \alpha) \sin(\psi) + V_{\mathrm{w}y} \tag{32}$$

$$\dot{h} = V_{\mathrm{a}} \sin(\theta - \alpha). \tag{33}$$

These equations of motion, however, are written in terms of MAV heading, ψ, rather than course, χ, which is the input to the system. It is desirable to express these equations of motion in terms of the inputs, V_{a}, χ, and θ. Because the equations of motion are already in terms of θ and V_{a}, we focus on the lateral (xy) plane. The wind triangle that relates ψ to χ is defined in the lateral plane as shown in Fig. 7.

Using the wind triangle relationship represented in Fig. 7 we can solve for the orientation of the airspeed vector, ψ, in terms of the system inputs: V_{a}, χ, and θ. The known quantities are the wind vector,$\boldsymbol{V}_{\mathbf{w}}$, the magnitude of the airspeed vector in the xy plane, $V_{\mathrm{a}} \cos(\theta - \alpha)$, and the direction of the groundspeed vector, χ. The wind triangle can be solved by ray-circle intersection similar to that outlined in Sec. III. The unit vector in this case is given by

$$\begin{bmatrix} u_{\mathrm{p}x} & u_{\mathrm{p}y} & 0 \end{bmatrix}^{\mathsf{T}} = \begin{bmatrix} \cos(\chi) & \sin(\chi) & 0 \end{bmatrix}^{\mathsf{T}} \tag{34}$$

The point of intersection is found by projecting along the vector $[u_{\mathrm{p}x} \quad u_{\mathrm{p}y} \quad 0]^{\mathsf{T}}$ by d_2, where d_2 is given by

$$d_2 = V_{\mathrm{w}x} c_\chi + V_{\mathrm{w}y} s_\chi + \sqrt{V_{\mathrm{w}x}^2 c_\chi^2 + V_{\mathrm{w}x} V_{\mathrm{w}y} c_\chi s_\chi + V_{\mathrm{w}y}^2 s_\chi^2 + (V_{\mathrm{a}} c_{(\theta-\alpha)})^2 - V_{\mathrm{w}x}^2 - V_{\mathrm{w}y}^2} \tag{35}$$

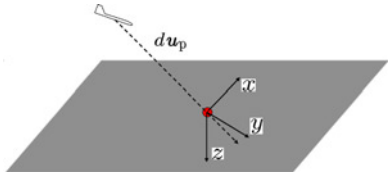

Fig. 6 Three-dimensional coordinate system (x is north, y is east, z is down).

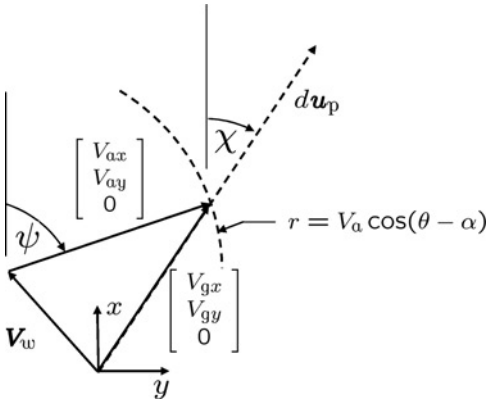

Fig. 7 Wind triangle in the lateral (xy) coordinate plane. Two sides and one angle of the triangle are known.

and c_x and s_x refer to $\cos(x)$ and $\sin(x)$ respectively. The value of d_2 represents the magnitude of the projection of the groundspeed vector onto the lateral plane,

$$d_2 = V_{\mathrm{g}} \cos(\gamma_{\mathrm{g}}) \tag{36}$$

The value of ψ can be determined from the point of intersection as

$$\psi = \mathrm{atan2}[d_2 \sin(\chi) - V_{\mathrm{w}y}, d_2 \cos(\chi) - V_{\mathrm{w}x}] \tag{37}$$

Substituting this expression into the equations of motion given in Eqs (31) through (33) gives the equations of motion in terms of the control inputs

$$\dot{x} = V_{\mathrm{a}} \cos(\theta - \alpha) \cos\{\mathrm{atan2}[d_2 \sin(\chi) - V_{\mathrm{w}y}, d_2 \cos(\chi) - V_{\mathrm{w}x}]\} + V_{\mathrm{w}x} \tag{38}$$

$$\dot{y} = V_{\mathrm{a}} \cos(\theta - \alpha) \sin\{\mathrm{atan2}[d_2 \sin(\chi) - V_{\mathrm{w}y}, d_2 \cos(\chi) - V_{\mathrm{w}x}]\} + V_{\mathrm{w}y} \tag{39}$$

$$\dot{h} = V_{\mathrm{a}} \sin(\theta - \alpha) \tag{40}$$

In three dimensions the values for $\hat{\chi}_{\mathrm{tgt}}$ and $\hat{\gamma}_{\mathrm{tgt}}$ are given by

$$\hat{\chi}_{\mathrm{tgt}} = \mathrm{atan2}(\hat{u}_{\mathrm{p}y}, \hat{u}_{\mathrm{p}x}) \tag{41}$$

$$\hat{\gamma}_{\mathrm{tgt}} = \sin^{-1}(\hat{u}_{\mathrm{p}h}). \tag{42}$$

Using Eqs (41) and (42) to compute $\hat{\chi}_{\mathrm{tgt}}$ and $\hat{\gamma}_{\mathrm{tgt}}$, the control law given by Eqs (10) and (29) can be used together to control the MAV for the case where wind speed is negligible (a rare case for MAVs).

The modification of the control law to account for the case where the wind speed is significant follows closely the analysis in Sec. III. As in Sec. III, it is assumed that there is no wind component in the z direction. This leads to a problem similar to that presented in Sec. III. The wind vector and the magnitude of the airspeed vector are known, and the goal is to find the airspeed vector that aligns the groundspeed vector with $\hat{\boldsymbol{u}}_{\mathbf{p}}$. In two dimensions this problem was solved by ray-circle intersection. In three dimensions this problem is solved by ray-sphere intersection. As with the 2D case, the ray is defined as a projection along the unit vector $\hat{\boldsymbol{u}}_{\mathbf{p}}$ of magnitude d_3. The sphere is centered at the tip of the wind speed vector and has a radius equal to V_{a}. The solution of the ray-sphere intersection problem proceeds similarly to that of the ray-circle intersection. The solution is given by

$$\boldsymbol{V}_{\mathbf{g}}^{\mathbf{d}} = d_3 \hat{\boldsymbol{u}}_{\mathbf{p}}, \tag{43}$$

where

$$d_3 = \hat{V}_{\mathrm{w}x}\hat{u}_{\mathrm{p}x} + \hat{V}_{\mathrm{w}y}\hat{u}_{\mathrm{p}y} + \sqrt{V_{\mathrm{a}}^2 - \hat{V}_{\mathrm{w}x}^2\left(\hat{u}_{\mathrm{p}y}^2 + \hat{u}_{\mathrm{p}h}^2\right) - \hat{V}_{\mathrm{w}y}^2\left(\hat{u}_{\mathrm{p}x}^2 + \hat{u}_{\mathrm{p}h}^2\right) - \hat{V}_{\mathrm{w}x}\hat{V}_{\mathrm{w}y}\hat{u}_{\mathrm{p}x}\hat{u}_{\mathrm{p}y}} \tag{44}$$

Once $\boldsymbol{V}_{\mathbf{g}}^{\mathbf{d}}$ has been determined, the desired airspeed vector can be calculated according to Eq. (23). γ_a^d can then be calculated from $\boldsymbol{V}_{\mathbf{a}}^{\mathbf{d}}$ as

$$\gamma_a^d = \sin^{-1}\left(\frac{V_{ah}^d}{\|\boldsymbol{V}_{\mathbf{a}}^{\mathbf{d}}\|}\right). \tag{45}$$

Using this value for γ_{a}^d, Eqs (29) and (25) can be used as the lateral and longitudinal control laws respectively. These control laws result in accurate landing at the target point provided the errors, $\tilde{\theta}$ and $\tilde{\chi}$, are acceptably small and the target is stationary.

Moving targets can be accounted for using the pseudo-wind introduced in Sec. IV. In three dimensions, pseudo-wind is defined as

$$\bar{\boldsymbol{V}}_{\mathbf{w}} = \begin{bmatrix} (\hat{V}_{\mathrm{w}x} - \hat{\dot{x}}_{\mathrm{tgt}}) & (\hat{V}_{\mathrm{w}y} - \hat{\dot{y}}_{\mathrm{tgt}}) & 0 \end{bmatrix}^{\mathsf{T}} \tag{46}$$

Introducing the new variable $\bar{d}$, and rewriting Eq. (44) in terms of the components of the pseudo-wind, $\bar{V}_{\mathrm{w}x}$ and $\bar{V}_{\mathrm{w}y}$, gives

$$\bar{d} = \bar{V}_{\mathrm{w}x}\hat{u}_{\mathrm{p}x} + \bar{V}_{\mathrm{w}y}\hat{u}_{\mathrm{p}y} + \sqrt{V_{\mathrm{a}}^2 - \bar{V}_{\mathrm{w}x}^2\left(\hat{u}_{\mathrm{p}y}^2 + \hat{u}_{\mathrm{p}h}^2\right) - \bar{V}_{\mathrm{w}y}^2\left(\hat{u}_{\mathrm{p}x}^2 + \hat{u}_{\mathrm{p}h}^2\right) - \bar{V}_{\mathrm{w}x}\bar{V}_{\mathrm{w}y}\hat{u}_{\mathrm{p}x}\hat{u}_{\mathrm{p}y}} \tag{47}$$

Once $\bar{d}$ has been determined, it can be used to compute the pseudo-wind-adjusted desired groundspeed vector, $\bar{\boldsymbol{V}}_{\mathbf{g}}^{\mathbf{d}}$, as

$$\bar{\boldsymbol{V}}_{\mathbf{g}}^{\mathbf{d}} = \bar{d}\hat{\boldsymbol{u}}_{\mathbf{p}} \tag{48}$$

The pseudo-wind-adjusted desired airspeed vector $\bar{\boldsymbol{V}}_{\mathbf{a}}^{\mathbf{d}}$ can then be computed as

$$\bar{\boldsymbol{V}}_{\mathbf{a}}^{\mathbf{d}} = \bar{\boldsymbol{V}}_{\mathbf{g}}^{\mathbf{d}} - \bar{\boldsymbol{V}}_{\mathbf{w}} \tag{49}$$

This value can then be used to compute the pseudo-wind-corrected value of γ_{a}^d as

$$\bar{\gamma}_{\mathrm{a}}^d = \sin^{-1}\left(\frac{\bar{V}_{ah}^d}{\|\bar{\boldsymbol{V}}_{\mathbf{a}}^{\mathbf{d}}\|}\right). \tag{50}$$

Finally, the longitudinal control law given by Eq. (25) can be rewritten in terms of $\bar{\gamma}_{\mathrm{a}}^d$ as

$$\theta^c = \bar{\gamma}_a^d + \hat{\alpha} + \bar{\theta}. \tag{51}$$

Because the lateral control given by Eq. (29) is insensitive to wind, it must be modified to take into account the moving target. The correct value of χ^c is given by the orientation of the groundspeed vector which results from tracking $\bar{\boldsymbol{V}}_{\mathbf{a}}^{\mathbf{d}}$ in the presence of the estimated wind, $\hat{\boldsymbol{V}}_{\mathbf{w}}$ (not the pseudo-wind $\bar{\boldsymbol{V}}_{\mathbf{w}}$). This leads to the expression for the desired groundspeed vector

$$\boldsymbol{V}_{\mathbf{g}}^{\mathbf{d}} = \bar{\boldsymbol{V}}_{\mathbf{a}}^{\mathbf{d}} + \hat{\boldsymbol{V}}_{\mathbf{w}} \tag{52}$$

The orientation of this vector in the lateral plane is given by

$$\chi^c = \mathrm{atan2}(\bar{V}_{\mathrm{a}y}^d + \hat{V}_{\mathrm{w}y},\, \bar{V}_{\mathrm{a}x}^d + \hat{V}_{\mathrm{w}x}). \tag{53}$$

This represents the lateral control law that results in accurate landing on a moving target in the presence of wind. It is important to note that for the case where the pseudo-wind is equal to zero, meaning the target is stationary, this control law gives the same result as Eq. (29).

The trajectories resulting from integrating the equations of motion given in Eqs (38) through (40) subject to the longitudinal and lateral control laws given in Eqs (51) and (53) are shown in Fig. 8. Glideslopes are shown for values of $\tilde{\theta}$ and $\tilde{\chi}$ ranging from $-15°$ each to $15°$ each. It can be seen from Fig. 8 that the same effects that were observed in the 2D case are observed in the three-dimensional (3D) case. Errors cause the glideslope to deviate from the nominal linear glideslope, but relatively large errors can be tolerated without significantly affecting the landing point.

VII. Bias Correction

The analysis to this point has focused on feedback control that does not correct for the effects of bias errors. Significant bias error, however, can result from a number of sources including relative orientation estimation error, parameter estimation error, target velocity estimation error, and wind estimation error. In the presence of these errors, the feedback control law may still result in accurate landing at the target location. However, the trajectory followed to the target will deviate from the nominal linear trajectory. The amount of deviation is a function of the magnitude

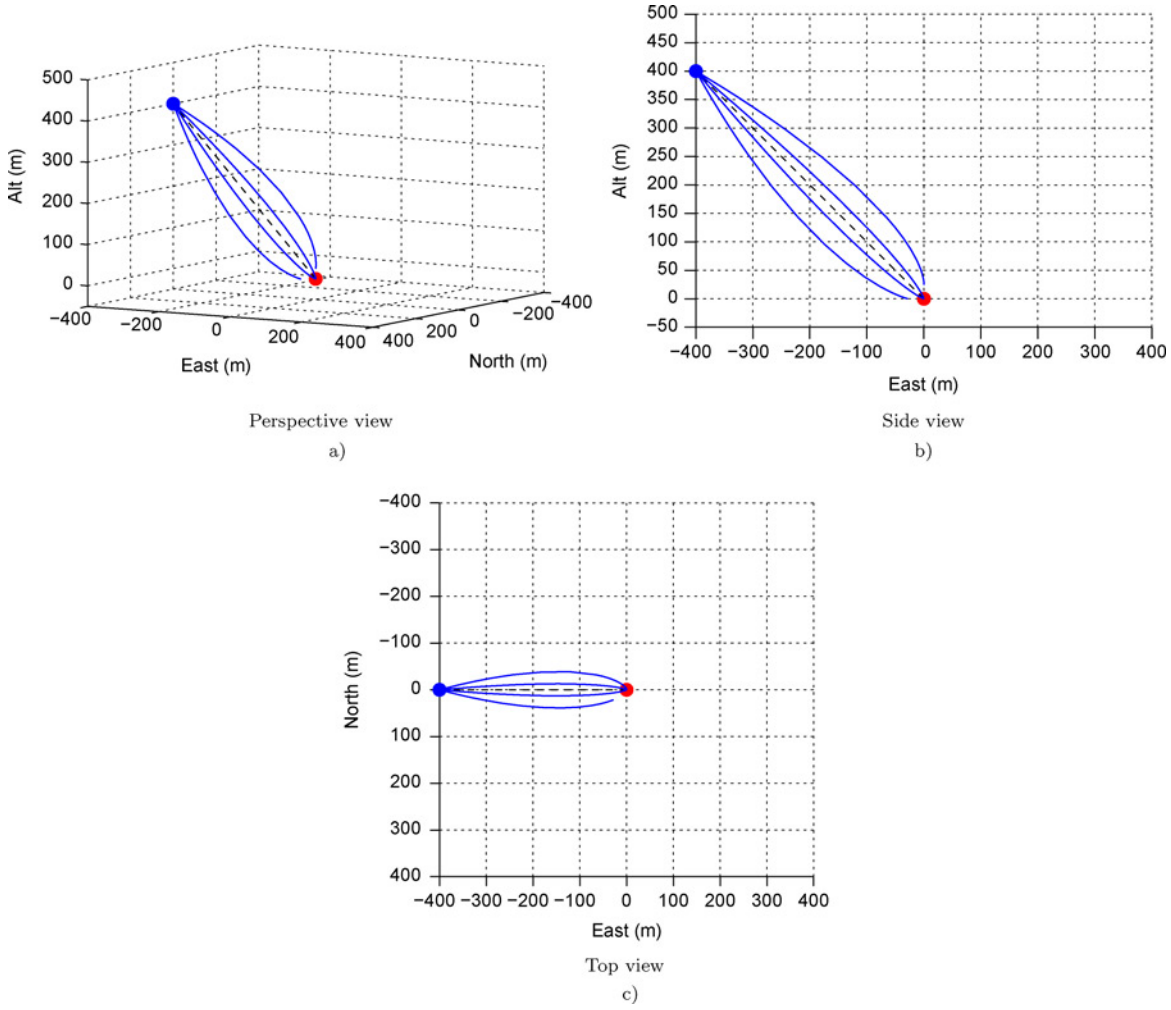

Fig. 8 The effect of errors, $\tilde{\theta}$ and $\tilde{\chi}$ on landing trajectory. The nominal linear glideslope is represented by the dashed line. The most shallow glideslope corresponds to $\tilde{\theta} = -15°$, $\tilde{\chi} = -15°$. The steepest glideslope corresponds to $\tilde{\theta} = 15°$, $\tilde{\chi} = 15°$. The intermediate glideslopes represent 10° increments in each error term.

of the bias errors and can result in significant undershoot or overshoot. For this reason, it is desired to design a bias correction that is able to overcome the effects of these biases. This adaptive bias correction is represented schematically in Fig. 1.

Examination of each of the possible error sources leads to the definition of three different error terms. The first term, μ, represents the error in tracking the desired linear trajectory. The second and third terms, ν_{lat} and ν_{lon}, represent the error in correctly generating the desired trajectory. Each of these error terms is assumed to be a random variable whose distribution is a non-zero mean Gaussian. The bias of the distribution is unknown but assumed to be constant, or at least slowly varying. The goal of the bias estimator is to determine the bias component of the error while filtering the high-frequency noise content.

The first bias term, μ, is caused by both parameter estimation errors and wind estimation errors. This tracking error affects only the longitudinal control, because the orientation of the MAV's lateral velocity vector χ is an input to the system. For the longitudinal control, however, the parameter α must be estimated to correctly choose θ^c given $\bar{\gamma}_{\text{a}}^d$ (see Eq. (51)). In addition, if the wind has not been estimated correctly, then the lateral component of the actual groundspeed vector will be different than the anticipated lateral component of the groundspeed vector. At the

same time, the longitudinal component of the groundspeed vector remains $V_a \sin(\theta - \alpha)$. This results in an actual glideslope angle that deviates from the desired glideslope angle. The value of μ is defined as the difference between these glideslope angles. This value can be estimated using the desired groundspeed vector $\boldsymbol{V}_{\mathbf{g}}^{\mathbf{d}}$ and estimated actual groundspeed vector $\hat{\boldsymbol{V}}_{\mathbf{g}}^{\mathbf{a}}$ as

$$\hat{\mu} = \sin^{-1}\left(\frac{V_{gh}^{d}}{\|\boldsymbol{V}_{\mathbf{g}}^{\mathbf{d}}\|}\right) - \sin^{-1}\left(\frac{\hat{V}_{gh}^{a}}{\|\hat{\boldsymbol{V}}_{\mathbf{g}}^{\mathbf{a}}\|}\right). \tag{54}$$

The second and third error terms, ν_{lat} and ν_{lon}, represent the errors in correctly selecting the desired trajectory, $\boldsymbol{V}_{\mathbf{g}}^{\mathbf{d}}$. If the target is known to be stationary, these error terms are affected only by relative orientation estimation error. If the target is moving, these error terms are also affected by wind estimation errors and target velocity estimation errors. To see how this error term can be calculated, consider the longitudinal case shown in Fig. 9. Given measurements at two different times, t_1 and t_2, we can develop an approximate expression for ν_{lon}. First, we define ν_{lon} in terms of γ_{g}^{d} as

$$\nu_{\text{lon}} = \gamma_{\text{g}}^{d} - \gamma_{\text{tgt}} \tag{55}$$

where γ_{tgt} represents the orientation of the motion vector that, if tracked, would result in a linear landing trajectory. Next, we define the angle β as shown in Fig. 9. Given the assumption that the bias component of ν_{lon} varies slowly in time, we can write an expression for β as

$$\beta \approx \gamma_{\text{g}}^{d}(t_2) - \gamma_{\text{g}}^{d}(t_1) \tag{56}$$

where γ_{g}^{d} is given by

$$\gamma_{\text{g}}^{d} = \sin^{-1}\left(\frac{V_{gh}^{d}}{\|\boldsymbol{V}_{\mathbf{g}}^{\mathbf{d}}\|}\right) \tag{57}$$

and $\gamma_{\text{g}}^{d}(t)$ refers to the value of γ_{g}^{d} at time t.

Introducing the term λ to represent the distance to the target and κ to represent the linear distance traveled by the MAV between times t_1 and t_2, we can write another approximation involving β

$$\lambda\beta \approx \kappa \sin(\mu + \nu_{\text{lon}}). \tag{58}$$

Substituting the value for β given in Eq. (56) into this expression and solving for ν_{lon} gives

$$\nu_{\text{lon}} \approx \sin^{-1}\left(\frac{\lambda(\gamma_{\text{g}}^{d}(t_2) - \gamma_{\text{g}}^{d}(t_1))}{\kappa}\right) - \mu \tag{59}$$

The value of μ in this expression can be estimated using Eq. (54), and the values of λ and κ can be estimated from GPS. Thus Eq. (59) can be rewritten in terms of known or measurable quantities as

$$\hat{\nu}_{\text{lon}} = \sin^{-1}\left(\frac{\hat{\lambda}(\gamma_{\text{g}}^{d}(t_2) - \gamma_{\text{g}}^{d}(t_1))}{\hat{\kappa}}\right) - \hat{\mu} \tag{60}$$

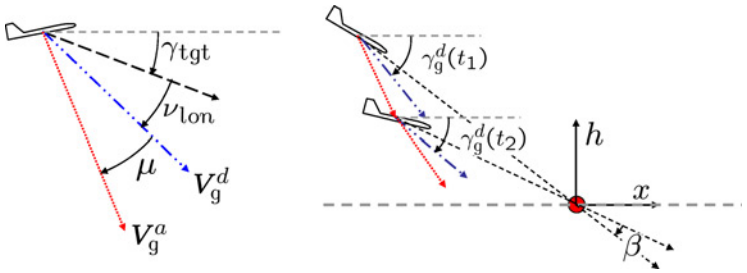

Fig. 9 Two-dimensional longitudinal tracking given the error terms μ and ν_{lon}.

Similar arguments can be used to derive an approximation for ν_{lat}. The main difference being that there is no μ component in the lateral direction for the reasons outlined above. In the lateral case, the estimate of the error term is given by

$$\hat{\nu}_{\text{lat}} = \sin^{-1}\left(\frac{\hat{\lambda}(\chi^d(t_2) - \chi^d(t_1))}{\hat{\kappa}}\right) \tag{61}$$

Having developed expressions for estimating the error terms μ, ν_{lat}, and ν_{lon} from known or measurable quantities, we now use these values to define the bias correction terms M, N_{lat}, and N_{lon}. These bias correction terms represent filtered estimates of the error terms μ, ν_{lat}, and ν_{lon}. These values are updated according to the differential equations

$$\dot{M} = k_1\hat{\mu} \tag{62}$$

$$\dot{N}_{\text{lat}} = k_2\hat{\nu}_{\text{lat}} \tag{63}$$

$$\dot{N}_{\text{lon}} = k_3\hat{\nu}_{\text{lon}}. \tag{64}$$

Correct selection of the gains k_1, k_2, and k_3 result in bias correction terms that capture the low frequency bias component of the error terms while attenuating the higher frequency components. These adaptive terms are then included in the control laws outlined in Sec. VI giving

$$\theta^c = \bar{\gamma}_{\text{a}}^d + \hat{\alpha} + \bar{\theta} + M + N_{\text{lon}} \tag{65}$$

$$\chi^c = \text{atan2}(\bar{V}_{\text{a}y}^d + \hat{V}_{\text{w}y}, \bar{V}_{\text{a}x}^d + \hat{V}_{\text{w}x}) + N_{\text{lat}}. \tag{66}$$

When θ^c or χ^c result in trajectories that are nonlinear, the error terms are nonzero. As long as the error terms are non-zero, the values of M, N_{lat}, and N_{lon} will adapt, thus forcing the commands closer to the commands that result in a linear trajectory.

The effect of adding these adaptive terms to the control law can be seen by integrating the equations of motion given by Eqs (38) through (40) subject to the control laws given in Eqs. (65) and (66). This can be seen in Fig. 10 which compares the performance of the feedback control law with bias correction to that of the feedback control law without bias correction. The calculation of the control inputs was subject to the following bias errors:

1) relative orientation estimation error: azimuth, 15°; elevation, 15°
2) wind estimation error: wind speed, 3 m/s; wind direction, 30°
3) target velocity estimation error: target speed, 3 m/s; target direction, 30°
4) parameter estimation error: α, 5°

The nominal conditions for this test were a wind speed of 4 m/s from the northeast (crosswind), a target speed of 4 m/s to the southeast, and a commanded airspeed of 13 m/s.

The trajectories shown in Fig. 10 demonstrate the ability of the bias correction to effectively reduce deviation from the nominal linear trajectory caused by bias errors. This allows larger magnitude bias errors to be tolerated by the system without significantly affecting landing accuracy.

Our approach assumes that the longitudinal and lateral dynamics can be decoupled and that control laws can be considered separately as in Eqs (65) and (66). The results of this paper support this assumption. It is probable, however, that performance could be improved by considering the coupling between longitudinal and lateral modes, especially under more demanding flight conditions such as those requiring high bank angles in significant crosswinds. While the current approach handles these conditions, explicit modeling of cross coupling effects would reduce the amount of adaptive bias correction needed and improve the system response.

VIII. Hardware Results

A. Hardware Testbed

Brigham Young University has developed a reliable and robust platform for testing unmanned air vehicles [16]. Fig. 11 shows the key elements of the testbed. The first frame shows the Procerus Kestrel autopilot (originally developed at BYU) which is equipped with a Rabbit 3400 29 MHz processor, rate gyros, accelerometers, and absolute and differential pressure sensors. The autopilot measures 3.8 × 5.1 × 1.9 cm and weighs 17 grams.

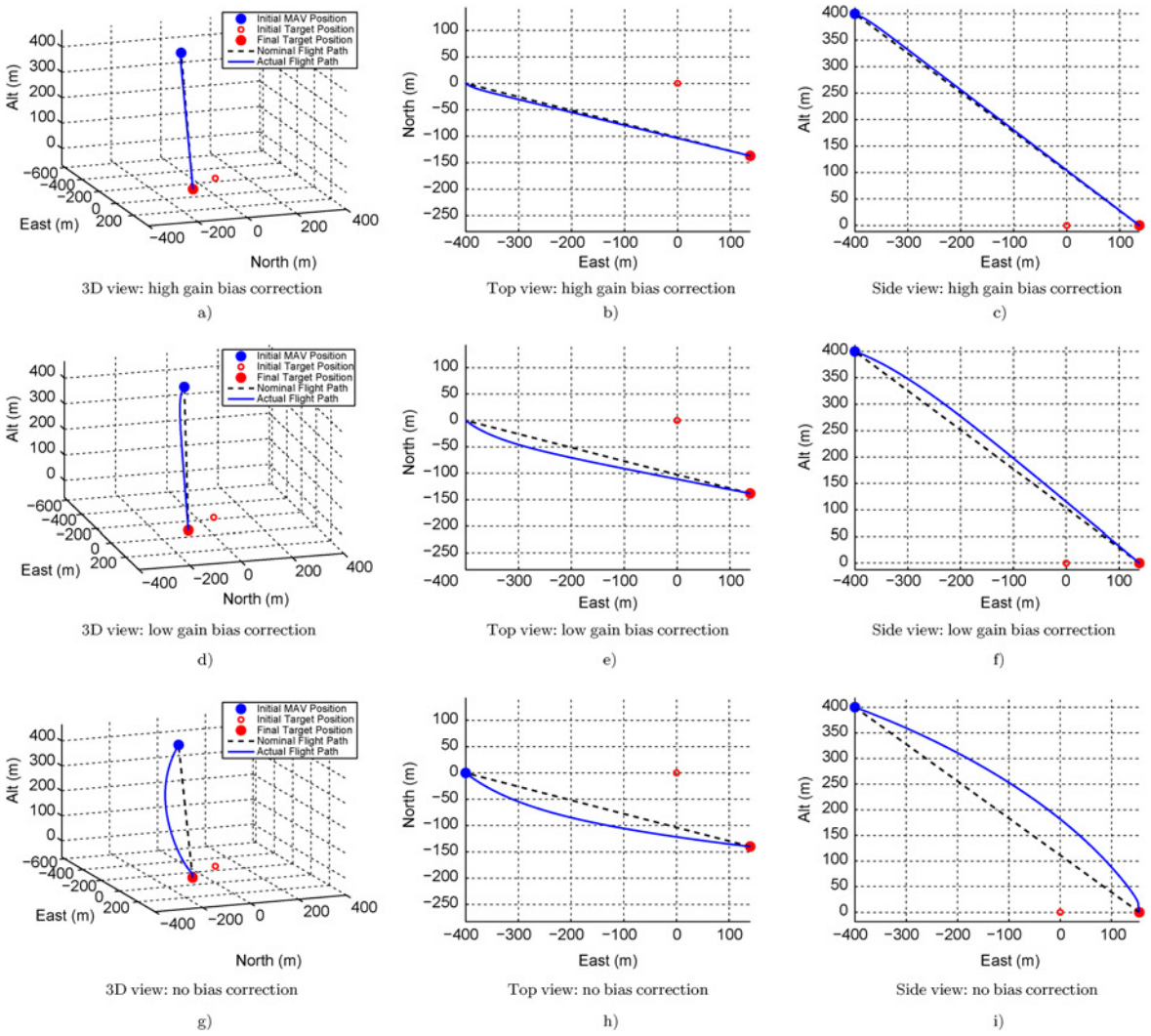

Fig. 10 Landing on a moving target in a crosswind. Comparison of trajectories generated using feedback control with high gain bias correction (top row), the feedback control with low gain bias correction (middle row), and feedback control without bias correction (bottom row).

The second frame in Fig. 11 shows one of the airframes used for the flight tests reported in this paper. The airframe is an elevon controlled flying wing designed by the BYU MAGICC Lab. It has a wingspan of 152 cm, a length of 58 cm, and a width of 12 cm. It weighs 1.1 kg unloaded and 2.0 kg fully loaded. It is propelled by a brushless electric motor which uses an electronic speed control and is fueled by four multicell lithium polymer batteries. Typical speeds for the aircraft are between 15 and 20 m/s (33 and 45 miles per hour). Maximum flight time for this aircraft is between 1 and 2 h depending on external conditions and the mission it is required to fly.

The third frame in Fig. 11 shows the ground station components. A laptop runs the Virtual Cockpit software that interfaces through a communication box to the MAV. An RC transmitter is used as a stand-by fail-safe mechanism to ensure safe operations.

The vision processing platform is shown in Fig. 12. The Helios platform is a small computing platform designed at BYU for real-time image processing in small autonomous vehicles. At the heart of the platform is a Xilinx Virtex-4 FX FPGA. The FPGA includes a PowerPC processor core as well as sophisticated reconfigurable logic. This platform combines the flexibility of a high-performance, embedded processor core with custom image processing hardware.

a) Kestrel autopilot b) MAV airframe c) Ground station components

Fig. 11 a) Kestrel autopilot. b) MAV airframe. c) Ground station components.

a) Helios

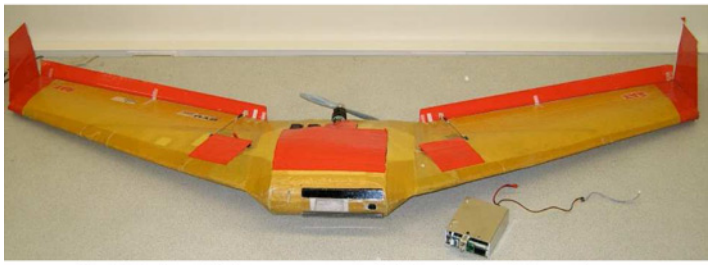

b) Helios board shown next to the MAV used for flight testing

Fig. 12 Flight test platform.

This vision processing platform meets the size, weight, and power requirements for use in hand-launchable MAVs. The Helios platform was mounted in the center payload bay of the MAV with the camera facing forward.

The proposed method is valid for both fixed and gimballed cameras. However, a fixed camera was used for all reported flight tests. The use of a fixed camera requires a wide-angle lens to keep the object of interest in the field of view, especially in high wind conditions where the MAV may have a significant crab angle. Even with a wide angle lens the control law itself does not explicitly ensure that the target remains in the camera's field of view. Because of this, both performance and robustness could be improved by using a gimballed camera to ensure lock on target and a narrow angle lens to allow target acquisition at a greater range to target.

B. Results and Discussion

The control law given by Eqs (65) and (66) was tested using the hardware platform described in Sec. A. The vision processing was done at full frame rate (30 Hz), but the control was only updated at 5 Hz. This update rate was chosen to demonstrate robustness to relatively slow update rates which would be required were the vision processing done off board. The control law was tested over a number of days with varying wind conditions. Flight data from two flights in very different wind conditions are shown in Figs. 13 and 14.

Figure 13 shows flight data from a flight in which the initial MAV landing coordinate was 30 m east of the target, and there was a tailwind at 80% of the commanded airspeed. A strong tailwind represents one of the more challenging

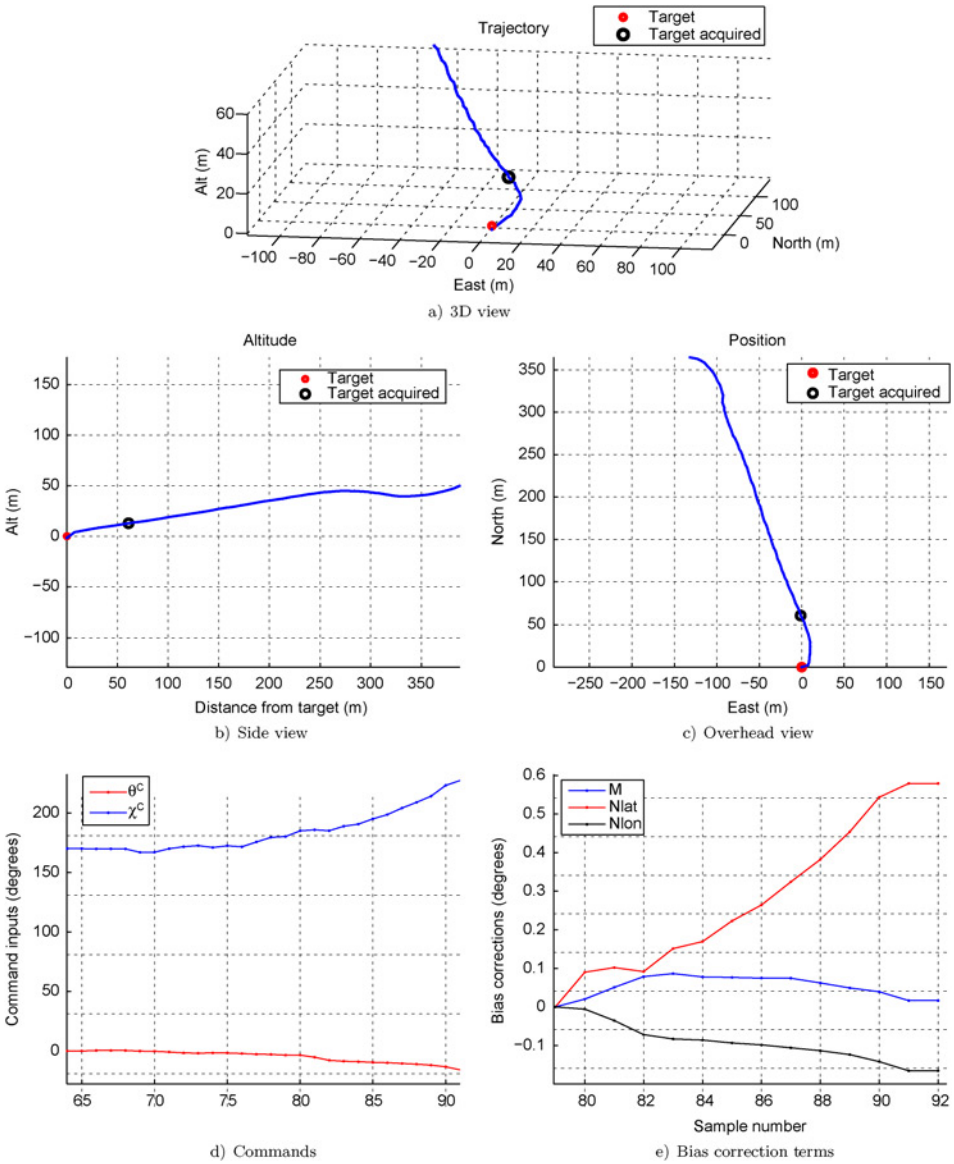

Fig. 13 Flight test results for landing on a stationary target in the presence of a tailwind at 80% of commanded airspeed.

scenarios for the vision-based landing algorithm because of the corresponding increase in MAV groundspeed. The increased groundspeed significantly reduces the amount of time between initial target acquisition and impact. For the data set shown, there were only 15 samples between initial acquisition and impact. This is compared with the 50 samples between initial acquisition and impact for the data set shown in Fig. 14. The relatively short time between initial acquisition and impact makes it difficult to estimate the biases in the system. Despite this difficulty, the control algorithm was able to repeatedly guide the MAV to within 0 to 5 m of the target.

Examination of Fig. 13 shows the large corrections that were required to guide the MAV to the target site. This can be seen from the aggressive change in flight path beginning at the point where the target was initially acquired. The fact that the pitch commands shown in Fig. 13(d) are continually decreasing indicates that the longitudinal misalignment correction should be negative. The total longitudinal misalignment correction is given by the sum of M and N_{lon}

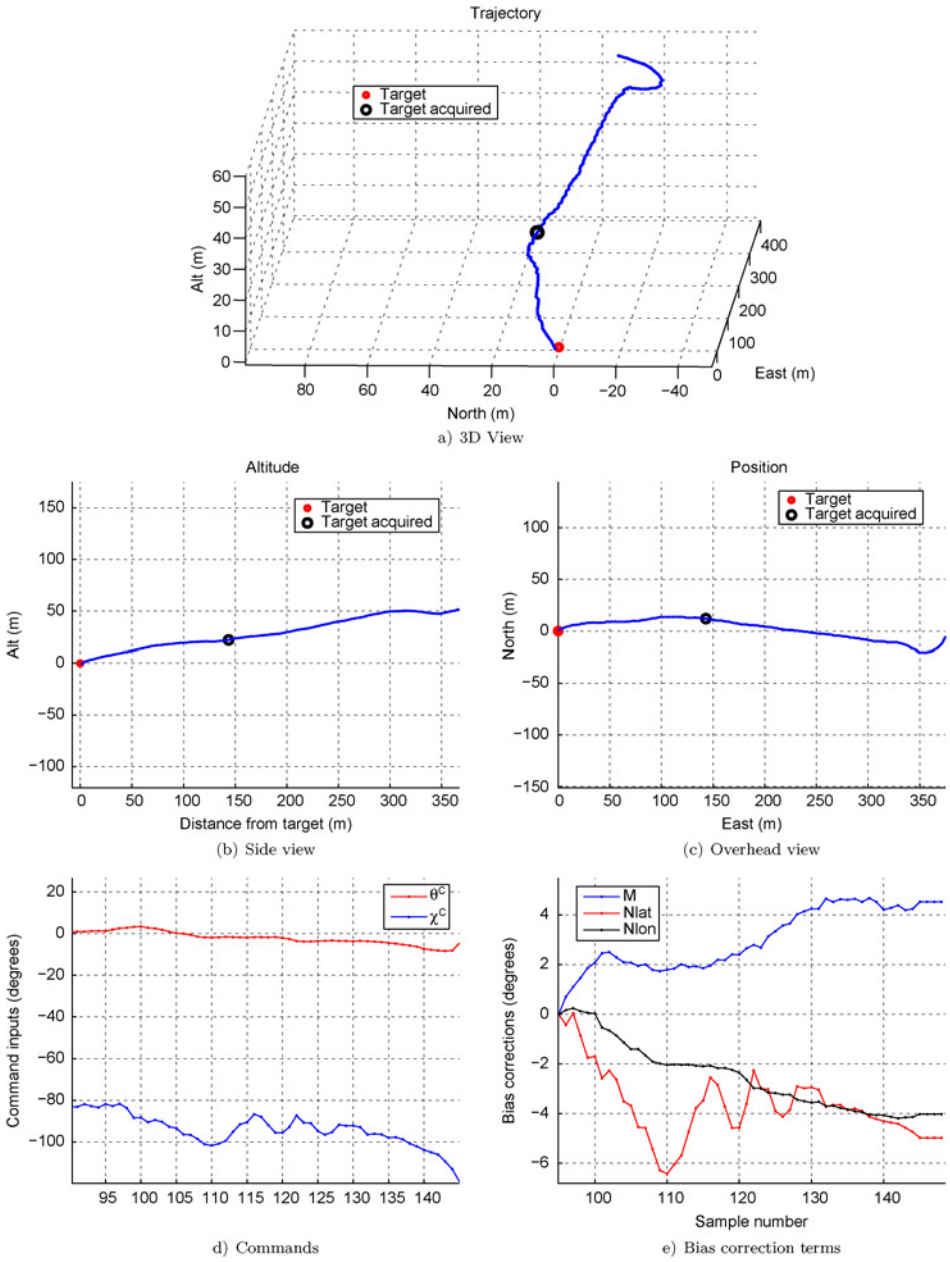

Fig. 14 Flight test results for landing on a stationary target in the presence of a headwind at 15% of commanded airspeed.

which indeed is negative, although the gains were not large enough to allow this term to make a meaningful difference. The continually increasing course commands shown in Fig. 13(d) indicate the lateral misalignment correction should be positive. Once again the sign of the bias correction term is accurate, although the gains should have been higher to allow this term to have greater effect.

Based on the results shown in Fig. 13, the bias estimation gains were increased by an order of magnitude, and more attempts at vision-guided landing were attempted on a subsequent day. The wind conditions on this second day of testing resulted in a relatively mild headwind at approximately 15% of commanded airspeed. Results from one

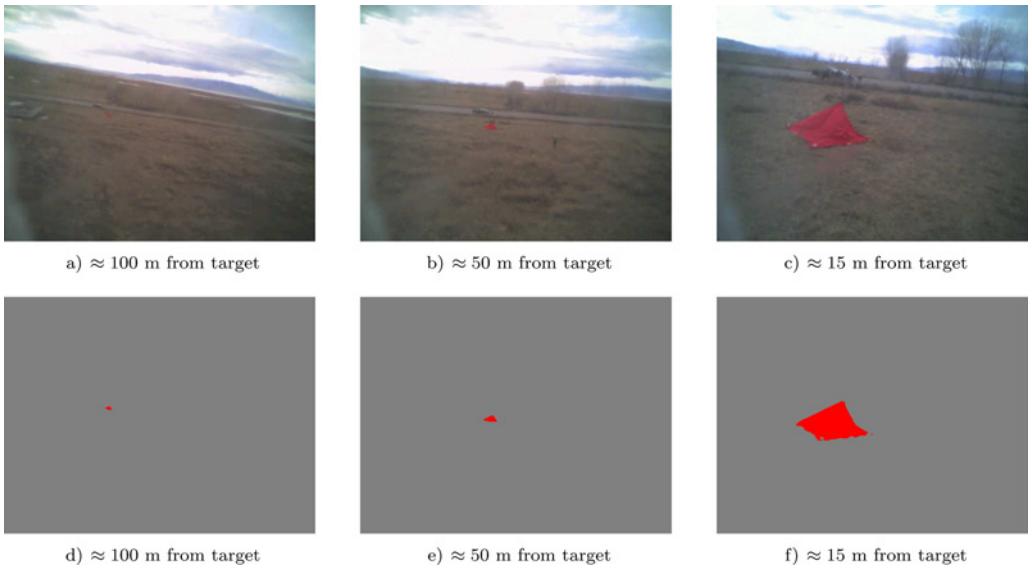

Fig. 15 Digital images of the target as captured by the Helios. The top row shows the raw images. The bottom row shows the processed images.

of the flight tests done on the second day of testing are shown in Fig. 14. In this test the MAV was given an initial landing point 20 m north and 20 m east of the true target location. It can be seen from Fig. 14 that immediately upon acquiring the target the MAV pulled up and to the south. This is the correct response as it was heading to a landing point that was short of the target and to the north.

Examining the MAV trajectory in the longitudinal plane (Fig. 14(b)) shows that the glideslope after target acquisition and initial correction was fairly linear. This indicates that there was relatively little total longitudinal misalignment. This is borne out by the fact that the total longitudinal misalignment ($M + N_{\text{lon}}$) hovers around zero. It is interesting to note that though there is significant parameter estimation error (given by M) and significant relative orientation estimation error (given by N_{lon}) these errors essentially cancel each other even as they adapt.

In the lateral plane, the fact that χ^c is continually decreasing in Fig. 14(d) indicates that the lateral bias correction term should be negative. This indeed is the case. Furthermore, because of the order of magnitude increase in bias estimation gains, this term was able to play a significant role in reducing deviation from the nominal linear trajectory. This in turn contributed to more accurate landing at the target site.

In total, 15 attempts at vision-guided landing were made on the second day of testing using the higher bias estimation gains. Of these attempts, twelve of the fifteen resulted in impact with the target. Of the three attempts that missed, each touched down within 5 m of the target.

The algorithm was also used to guide the MAV to a successful landing in the back of a pickup truck moving at an approximately known velocity. Still images captured using the Helios platform during a landing attempt on the stationary target are shown in Fig. 15. A sequence of images from the video footage of landing on a moving target are shown in Fig. 16.

IX. Conclusion

A control law was developed for using vision-based feedback to accurately land on fixed and moving targets in the presence of wind and bias errors. It was shown that for sufficiently small bias errors, vision-based feedback without bias estimation would result in accurate landing on a moving target. However, because bias errors can be introduced from a number of sources including relative orientation estimation error, parameter estimation error, wind estimation error, and target velocity estimation error, a scheme for estimating and correcting for bias errors was introduced. This bias correction scheme was shown to significantly reduce the deviations from the nominal linear glideslope caused by bias errors. The control scheme was tested in hardware flight tests using onboard vision processing and a

Fig. 16 Sequence of images showing successful landing on a moving platform.

stationary target. The control was deliberately run at only 5 Hz to demonstrate robustness to relatively slow update rates. The control scheme was able to guide the MAV to impact with a 2 m square target on 12 of 15 attempts. On all attempts, the MAV touched down within 5 m of the target center. The method was also used to successfully land a MAV in the back of a pickup truck moving at an approximately known velocity. The algorithm demonstrated similar performance under a variety of wind conditions including significant tailwinds, crosswinds, and headwinds.

References

[1] Barber, D. B., Redding, J. D., McLain, T. W., Beard, R. W., and Taylor, C. N., "Vision-based Target Geo-location using a Fixed-wing Miniature Air Vehicle," *Journal of Intelligent and Robotic Systems*, Vol. 47, No. 4, 2006, pp. 361–382. doi: 10.1007/s10846-006-9088-7

[2] Saripalli, S., Montgomery, J., and Sukhatme, G., "Visually Guided Landing of an Unmanned Aerial Vehicle," *IEEE Transactions on Robotics and Automation*, Vol. 19, No. 3, 2003, pp. 371–380. doi: 10.1109/TRA.2003.810239

[3] Shakernia, O., Vidal, R., Sharp, C. S., Ma, Y., and Sastry, S., "Multiple View Motion Estimation and Control for Landing an Unmanned Aerial Vehicle," *Proceedings of the IEEE International Conference on Robotics and Automation*, IEEE Publications, Piscataway, NJ, 2002, pp. 2793–2798.

[4] Saripalli, S., Montgomery, J., and Sukhatme, G., "Vision-based Autonomous Landing of an Unmanned Aerial Vehicle," *Proceedings of the IEEE International Conference on Robotics and Automation ICRA'02*, Vol. 3, IEEE Publications, Piscataway, NJ, 2002.

[5] Saripalli, S., and Sukhatme, G., "Landing on a Moving Target using an Autonomous Helicopter," *Proceedings of the International Conference on Field and Service Robotics,* July, 2003.

[6] Hintze, J., Christian, D., Theodore, C., Tischler, M., and McLain, T., "Automated Landing of a Rotorcraft UAV in a Non-cooperative Environment," *Proceedings of the 60th Annual Forum of the American Helicopter Society*, Baltimore, MD, AHS International, Alexandria, VA, June 2004.

[7] Hintze, J., *Autonomous Landing of a Rotary Unmanned Aerial Vehicle in a Non-Cooperative Environment Using Machine Vision*, Master's thesis, Brigham Young University, April 2004.

[8] Yakimenko, O., Kaminer, I., Lentz, W., and Ghyzel, P., "Unmanned Aircraft Navigation for Shipboard Landing Using Infrared Vision," *IEEE Transactions on Aerospace and Electronic Systems*, Vol. 38, No. 4, 2002, pp. 1181–1200. doi: 10.1109/TAES.2002.1145742

[9] Frezza, R., and Altafini, C., "Autonomous Landing by Computer Vision: An Application of Pathfollowing in SE (3)," *Proceedings of the 39th IEEE Conference on Decision and Control*, Vol. 3, 2000.

[10] Chahl, J., Srinivasan, M., and Zhang, S., "Landing Strategies in Honeybees and Applications to Uninhabited Airborne Vehicles," *The International Journal of Robotics Research*, Vol. 23, No. 2, 2004, pp. 101–110.
doi: 10.1177/0278364904041320

[11] Barrows, G., and Neely, C., "Mixed-mode VLSI Optic Flow Sensors for In-flight Control of a Micro Air Vehicle," *Proceedings SPIE*, San Diego, CA, August 2000, pp. 52–63.

[12] Zufferey, J.-C., and Floreano, D., "Toward 30-gram Autonomous Indoor Aircraft: Vision-based Obstacle Avoidance and Altitude Control," *Proceedings of the IEEE International Conference on Robotics and Automation*, IEEE Publications, Piscataway, NJ, 2005, pp. 2594–2599.

[13] Ruffier, F., and Franceschini, N., "Visually Guided Micro-Aerial Vehicle: Automatic Take Off, Terrain Following, Landing and Wind Reaction," *Proceedings of the IEEE International Conference on Robotics and Automation*, IEEE Publications, Piscataway, NJ, 2004, pp. 2339–2346.

[14] Barrows, G. L., Chahl, J. S., and Srinivasan, M. V., "Biomimetic Visual Sensing and Flight Control," *The Aeronautical Journal, London: The Royal Aeronautical Society*, Vol. 107, No. 1069, 2003, pp. 159–168.

[15] Barber, D., Griffiths, S., McLain, T., and Beard, R., "Autonomous Landing of Miniature Aerial Vehicles," *Infotech@ Aerospace*, 2005, pp. 1–14.

[16] Beard, R., Kingston, D., Quigley, M., Snyder, D., Christiansen, R., Johnson, W., et al., "Autonomous Vehicle Technologies for Small Fixed Wing UAVs," *AIAA Journal of Aerospace Computing, Information, and Communication*, Vol. 2, No. 1, January 2005, pp. 92–108.
doi: 10.2514/1.8371

Kelly Cohen
Associate Editor